Applied Mathematical Modelling 53 (2018) 369–383

Contents lists available at ScienceDirect

Applied Mathematical Modelling

journal homepage: www.elsevier.com/locate/apm

External force-induced focus pattern of a flexible filament in a viscous fluid

Yuan-Qing Xu[a,b], Ming-Yi Wang[a,b], Qiong-Yao Liu[a,b], Xiao-Ying Tang[a,b], Fang-Bao Tian[c,*]

[a] School of Life Science, Beijing Institute of Technology, Beijing 100081, China
[b] Key Laboratory of Convergence Medical Engineering System and Healthcare Technology, The Ministry of Industry and Information Technology, Beijing Institute of Technology, Beijing 100081, China
[c] School of Engineering and Information Technology, University of New South Wales, Canberra ACT 2600, Australia

ARTICLE INFO

Article history:
Received 26 April 2016
Revised 25 August 2017
Accepted 4 September 2017
Available online 13 September 2017

Keywords:
Immersed boundary
Lattice Boltzmann method
Focus pattern
Vibrating filament

ABSTRACT

In order to study the mechanism of wall attraction of micro-swimmers, this paper presents a numerical study on the external force-induced focus of a flexible filament in a quiescent viscous fluid. In the numerical model, the fluid is solved by the lattice Boltzmann method (LBM) and the moving filament is modeled with the immersed boundary (IB). The filament is parallel and adjacent to a near-wall initially. A periodic driving force is applied on it to induce a vibration motion which could lead to the wall attraction phenomenon of the vibrating filament. Furthermore, by adjusting the mean value of the periodic driving force, we can get a stable vibrating mode of the filament, which is called as focus pattern. The pattern is a special state of the wall attraction, which provides a convenient way to investigate the law of hydrodynamic balance. Simulations are conducted by varying the following parameters, including the boundary setting of the flow field, the magnitude, period and waveform of the external driving force, the bending modulus of the filament and the fluid viscosity. The laws of the focus pattern are discussed in detail. The results indicate that all the above parameters can affect the focus position remarkably. By analyzing the outputs of each item of the Navier–Stokes momentum conservation equation, we found that the focus is mainly caused by the balance of the joint force on the filament and the pressure effect from the flow. This finding may provide a novel way to uncover the hydrodynamic mechanism for wall attraction of waving propulsion.

1. Introduction

Some micro-swimmers, like flagellar bacterium and animal sperm, can beat their cilia or tail to generate a propulsive force to swim in a fluid, this waving propulsion phenomenon is interesting, and the corresponding dynamics is a long-run concern topic in the fields of biology and engineering since it provides an inspiration for developing some underwater bionics equipment [1–3]. In the past studies of the motility of micro-swimmer, people found that waving propulsion near a wall or not might result in a remarkable difference in their swimming behaviors. According to some experimental studies, when human or some animal sperms are swimming near a wall, they may have a trend to be trapped by the wall and

* Corresponding author.
E-mail addresses: f.tian@adfa.edu.au, fangbao.tian@unsw.edu.au, onetfbao@gmail.com (F.-B. Tian).

http://dx.doi.org/10.1016/j.apm.2017.09.001
0307-904X/

swim along with it, this is known as the sperm accumulation near a boundary [4,5]. Moreover, it is also reported that the swimming sperm near a boundary not only can increase its forward efficiency [6,7], but also can take it as a boundary-following navigation to reach the egg [8]. Therefore, it is significant to investigate the formation of sperm accumulation and its mechanism.

Rothschild [4] observed that the distribution of bull sperm in a drop of sperm suspension tended to accumulate near the surface of the glass plates, and he suggested this might be due to a hydrodynamic interaction. Winet et al. [9] studied the response of human spermatozoa to gravity, boundaries and fluid shear. They found that the most influential stimulus was the solid boundaries, at which the sperm accumulated. Fauci and McDonald [10] simulated the sperm motility in the presence of solid and elastic walls. Their results also demonstrated the tendency of a near-wall to attract organisms. In recent years, with the rapid development of computer science and numerical method, some more effective models were proposed to study the details of the sperm accumulation. Smith et al. [5] studied a three-dimensional flagellar waveforms sperm with both planar and 'elliptical helicoid' beating patterns. The results showed that the sperm accumulated at distances of approximately 8.5–22 μm from surfaces, where the sperm can swim along the wall steadily, this finding indicates that the hydrodynamics factor may be the primarily causation for the wall attraction. Elgeti et al. [11] proposed a mesoscale simulation model to study the behaviors of swimming sperm near a wall, they also noted that the wall attraction of the sperm was caused by the hydrodynamics interaction between the beating tail and the wall.

According to the above studies, it can be deduced that the hydrodynamics effects play a critical role on wall attraction, while some related important mechanisms still keep unrevealed up to now, little quantitative explanation is found to light us to catch sight of the details of the hydrodynamics effects. For instance, the particular effects of the pressure, the fluid viscosity, the beating strength and etc., are still unclear on the wall attraction. Therefore, the details of the hydrodynamics effects of the wall attraction are necessary to be further investigated.

In this paper, aiming at the exploration of the details of the hydrodynamics effects of the wall attraction, we constructed a 2D immersed boundary-Lattice Boltzmann method (IB-LBM) model to simulate the wall attraction in a quiescent viscous fluid. In the present study, a segment of the waving tail of a human sperm is chosen to study the wall attraction, in the simulation, it is modeled as a length of flexible filament. In order to simulate the periodic motion, a periodic external force is introduced to conduct a vibration of the filament. By regulating the force, we find if the time-averaged joint force is set to work against the wall attraction, the vibrating filament can perform a periodic motion pattern in a definite scope steadily, and the whole FSI system will fall into an equilibrium state, we named the corresponding motion of the filament as focus pattern, it means that the hydrodynamics indices involved in the Navier–Stokes equation, such as the external force and the pressure, have reached a steady state. This provides a convenient way for analyzing the hydrodynamic balance laws. Furthermore, by the aid of the model on the focus pattern, the effects of the boundary settings of flow field, the magnitude and the waveform of the periodic driving force, the position initialization and the bending modulus of the filament, and the viscous of the fluid are investigated quantitatively. By regulating the above indices or parameters, the mechanism of the focus pattern of the vibrating filament is dissected, and the results may help us to know what actually the most important hydrodynamics effect is to bring about the wall attraction.

The rest of this paper is organized as the following. The physical model definitions, the numerical description of the IB-LBM and the filament mechanics are described in Section 2. Section 3 gives the validation and the verification of our numerical method. Section 4 discusses and analyzes the focus laws of the vibrating filament under different critical parameters. Final conclusions are given in Section 5.

2. Physical model and numerical description

2.1. The physical model

According to the problem of wall attraction of micro-swimmers (i.e. the human sperm), the physical model is established in the scale of μm, the ambient fluid is assumed to be water. The sketch map of the model is shown in Fig. 1(a). A flexible filament is chosen as the segment of the waving slim body of the micro-swimmer, it is immersed in the fluid and put

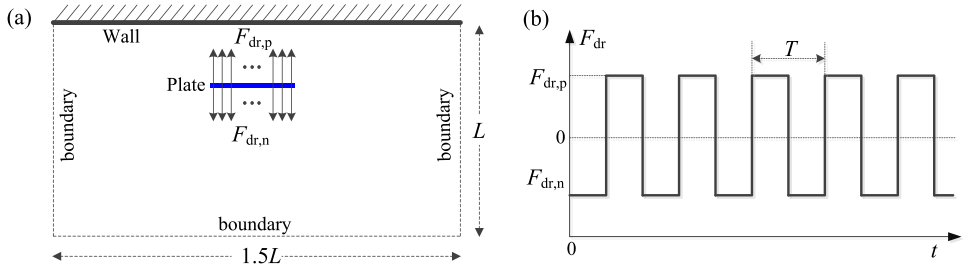

Fig. 1. The scheme of the simulation model and the setting of the driving force.

nearly at a planar wall. The density of the filament is assumed to be the same as that of the fluid, this allows us to treat the filament as massless in the modeling.

In the modeling, the dimensionless unit is used for all parameters. The default grid scale of the flow field is 300×200 ($1.5L \times L$) in the LBM frame, the length of the filament is $L_p = 0.25L$ (with 51 nodes, the spacing of two adjacent nodes is 1.0 Δx). Initialize the kinematic viscosity υ as 0.2 and the reference velocity U as 0.004. Therefore, the Reynolds number Re is about 1 ($Re = LU/\upsilon$). For the filament, the stretching coefficient $K_s = 500$, the bending modulus $K_b = 0.75$, it is initialized at a distance of $0.18L$ away from the wall. In order to impact a force to vibrate the filament, a square-wave force marked with F_{dr} is introduced as displayed in Fig. 1(a) and (b), in which the positive component of F_{dr} is $F_{dr,p}$ and the negative is $F_{dr,n}$. The period of the driving force $T = 6000\Delta t$, initialize $F_{dr,p} = 12.5$, $F_{dr,n} = -12.5$ for each node, where $F_{dr,p}$ and $F_{dr,n}$ are computed by $F_{dr,x} = F^*_{dr,x}/(\rho U^2)$, in which ρ is the fluid density and $F^*_{dr,x}$ is the force expression in LBM. The default total simulation time is $455T$. These parameters are used in the paper unless otherwise declared.

Based on the model, several critical aspects are picked up to study the law of the focus pattern of the vibrating filament, they are the boundary settings of the flow field, the magnitude, waveform and period of the driving force F_{dr}, the bending modulus K_b of the filament and the kinematic viscosity of the fluid υ.

2.2. The governing equations of the model

In the model, the filament is immersed in a viscous fluid, when it is driven into a vibration state, the ambient fluid will be enforced to flow, which is governed by the Navier–Stokes equations as

$$\rho \frac{\partial \boldsymbol{u}}{\partial t} + \rho \boldsymbol{u} \cdot \nabla \boldsymbol{u} = -\nabla p + \mu \nabla^2 \boldsymbol{u} + \boldsymbol{f} \text{ and } \nabla \cdot \boldsymbol{u} = 0, \tag{1}$$

where $\boldsymbol{u}$ is the velocity, μ is the kinetic viscosity of the fluid, $\boldsymbol{f}$ is the body force caused by the Lagrangian resultant force $\boldsymbol{F}$, and p is the pressure.

The filament is made up of a series of nodes connecting with springs in a consecutive way [12,13]. The dynamics of each node is governed by four forces, i.e. the stretching force $\boldsymbol{F}_s$, the bending force $\boldsymbol{F}_b$, the inertial force $\boldsymbol{F}_d$ and the external driving force $\boldsymbol{F}_{dr}$. Then we get the resultant force $\boldsymbol{F}$

$$\boldsymbol{F}(s,t) = \boldsymbol{F}_s(s,t) - \boldsymbol{F}_b(s,t) - \boldsymbol{F}_d(s,t) + \boldsymbol{F}_{dr}(s,t). \tag{2}$$

The stretching force $\boldsymbol{F}_s(s,t)$ follows the Hooke's law in the tangential direction, which is used to control the variation of the filament length. It can be calculated by [13,14]

$$\boldsymbol{F}_s(s,t) = \frac{\partial}{\partial s}\left[K_s\left(\left|\frac{\partial \boldsymbol{X}(s,t)}{\partial s}\right| - 1\right)\frac{\partial \boldsymbol{X}(s,t)}{\partial s}\right], \tag{3}$$

where K_s is the extensional coefficient, $\boldsymbol{X}$ is the coordinates of the filament and $\partial \boldsymbol{X}(s,t)/\partial s$ is the unit tangent vector.

The bending force, $\boldsymbol{F}_b(s,t)$, which expresses the bending moment of the filament in the normal direction, is derived from the Frechet derivative of the bending energy formula based on the virtual work principle [14,15]. It is

$$\boldsymbol{F}_b(s,t) = K_b \frac{\partial^4 \boldsymbol{X}(s,t)}{\partial s^4} \tag{4}$$

where K_b is the bending coefficient. In addition, for the end nodes of the filament, both the bending moment and transverse stress vanish, this requires [16,17]

$$\frac{\partial^2 \boldsymbol{X}(s,t)}{\partial s^2} = 0 \text{ and } \frac{\partial^3 \boldsymbol{X}(s,t)}{\partial s^3} = 0. \tag{5}$$

The inertial force of the particle nodes is [17]

$$\boldsymbol{F}_d(s,t) = S \frac{\partial^2 \boldsymbol{X}(s,t)}{\partial t^2}, \tag{6}$$

where S is the mass ratio of the filament. In the present study, because the density of the filament is assumed to be the same as its ambient fluid, this makes $S = 0$, that is the effect of $\boldsymbol{F}_d$ can be ignored.

2.3. The boundary conditions

As shown in Fig. 1(a), the upper boundary of the flow field is set as wall, on which the velocity is 0, and the pressure on all nodes of the boundary are set equally to that of the adjacent layer. The other three boundaries are set as free flow to simulate infinite flow condition approximately, where the velocities and the pressures both are set equally to the corresponding adjacent layer. In order to inspect the influences of the three boundary settings on the motion of the vibrating filament, different types of boundary settings are tested respectively, the results have been discussed in latter section. The similar boundary settings have been extensively used to study 2D micro-swimmers at low Reynolds number regime [6,7,10].

2.4. The numerical method IB-LBM

In the numerical model, the fluid dynamics formulized by the Navier–Stokes equations is solved by the two-dimensional nine-speed (D2Q9) lattice Boltzmann method [18], in which the discrete lattice Boltzmann equation with a single relaxation time model is [19,20]

$$g_i(\boldsymbol{x}+e_i\Delta t,\ t+\Delta t)-g_i(\boldsymbol{x},t)=-\frac{1}{\tau}\left[g_i(\boldsymbol{x},t)-g_i^{\mathrm{eq}}(\boldsymbol{x},t)\right]+\Delta t G_i, \tag{7}$$

where $g_i(\boldsymbol{x},t)$ is the distribution function for particles of velocity e_i at position $\boldsymbol{x}$ and moment t,Δt is the time step, g_i^{eq} is the equilibrium distribution function, τ is the non-dimensional relaxation time. For the D2Q9 lattice model, the nine particle velocities e_i are given by [19,20]

$$e_i=\begin{cases}(0,0),\ i=0\\ \left(\cos\left(\frac{i-1}{2}\pi\right),\sin\left(\frac{i-1}{2}\pi\right)\right)\frac{\Delta x}{\Delta t},\ i=1,2,3,4\\ \left(\cos\left(\frac{i-4.5}{2}\pi\right),\sin\left(\frac{i-4.5}{2}\pi\right)\right)\frac{\sqrt{2}\Delta x}{\Delta t},\ i=5,6,7,8\end{cases}, \tag{8}$$

where Δx is the lattice space. The settings of e_i enable a strategy to control the migration directions of the particle within one time step. In Eq. (1), the body force term G_i and the equilibrium distribution function g_i^{eq} are calculated by [21]

$$G_i=\left(1-\frac{1}{2\tau}\right)\omega_i\left[\frac{e_i-\boldsymbol{u}}{c_s^2}+\frac{e_i\cdot\boldsymbol{u}}{c_s^4}e_i\right]\cdot\boldsymbol{f}, \tag{9}$$

and

$$g_i^{eq}=\omega_i\rho\left[1+\frac{e_i\cdot\boldsymbol{u}}{c_s^2}+\frac{\boldsymbol{uu}:\left(e_ie_i-c_s^2\mathbf{I}\right)}{2c_s^4}\right], \tag{10}$$

where $\boldsymbol{f}$ is the body force density vector, and ω_i are the weights defined by $\omega_0=4/9$, $\omega_i=1/9$ for $i=1$ to 4 and $\omega_i=1/36$ for $i=5$ to 8. $C_s=\Delta x/\sqrt{3}\Delta t$ is the sound speed in LBM. The relaxation time τ relates with the kinematic viscosity υ of the flow in terms of Ref. [21]

$$\tau=\frac{\upsilon}{c_s^2\Delta t}+0.5. \tag{11}$$

Once the particle distribution function g_i is obtained, the fluid density ρ, the velocity $\boldsymbol{u}$ and the pressure p can be computed from [18,22]

$$\rho=\sum_i g_i, \tag{12}$$

$$\boldsymbol{u}=\frac{\sum_i g_i+0.5\boldsymbol{f}\Delta t}{\rho}, \tag{13}$$

and

$$P=\sum_i \rho c_s^2. \tag{14}$$

The non-equilibrium extrapolation method is used to obtain the particle distribution function on the boundaries, which is marked by $g_{i,\mathrm{b}}$ as [21]

$$g_{i,\mathrm{b}}(\boldsymbol{x},t)=g_{i,\mathrm{b}}^{\mathrm{eq}}(\boldsymbol{x},t)+(g_{i,\mathrm{n}}(\boldsymbol{x},t)-g_{i,\mathrm{n}}^{\mathrm{eq}}(\boldsymbol{x},t)), \tag{15}$$

where $g_{i,\mathrm{n}}$ represents the particle distribution function on the neighboring grid, $g_{i,\mathrm{b}}^{\mathrm{eq}}$ and $g_{i,\mathrm{n}}^{\mathrm{eq}}$ are respectively the equilibrium distribution functions of $g_{i,\mathrm{b}}$ and $g_{i,\mathrm{n}}$.

In the frame of the IB method, the Lagrangian force $\boldsymbol{F}$ is spread onto the collocated grid points near the boundary by Ref. [23]

$$\boldsymbol{f}(\boldsymbol{x},t)=\int_\Gamma \boldsymbol{F}(s,t)D(\boldsymbol{x}-\boldsymbol{X})\mathrm{d}s, \tag{16}$$

where $D(\boldsymbol{x}-\boldsymbol{X})$ is the Dirac's delta function, it is [23]

$$D(\boldsymbol{x}-\boldsymbol{X})=\delta(x-X)\delta(y-Y), \tag{17}$$

in which $\delta(x-X)$ is

$$\delta(x-X)=\begin{cases}\dfrac{1}{8\Delta x}\left(3-\dfrac{2|r|}{\Delta x}+\sqrt{1+\dfrac{4|r|}{\Delta x}-4\left(\left|\dfrac{r}{\Delta x}\right|\right)^2}\right), & |r|=|x-X|<\Delta x\\ \dfrac{1}{8\Delta x}\left(5-\dfrac{2|r|}{\Delta x}+\sqrt{-7+\dfrac{12|r|}{\Delta x}-4\left(\left|\dfrac{r}{\Delta x}\right|\right)^2}\right), & \Delta x\le|r|=|x-X|<2\Delta x\\ 0, & |r|=|x-X|\ge 2\Delta x\end{cases}, \tag{18}$$

where n is dimension number of the numerical problem, i is the serial number and h is the lattice space of the background grid for the flow.

Then the velocity of the filament $\boldsymbol{X}$ can be updated through [23,24]

$$\boldsymbol{U}(s,t)=\int_{\Omega}\boldsymbol{u}(\boldsymbol{x},t)D(\boldsymbol{x}-\boldsymbol{X})\mathrm{d}x, \tag{19}$$

and the position of the filament is updated by

$$\frac{\partial\boldsymbol{X}}{\partial t}=\boldsymbol{U}(s,t), \tag{20}$$

where $\boldsymbol{U}(s,\ t)$ is the velocity of filament.

3. Validation and verification

In the present study, the IB-LBM is employed to establish the numerical model. In order to verify and validate the model, two sections including the experimental and numerical comparisons are carried out to inspect the validity and accuracy of our model.

3.1. The passive vibration of a flexible filament in a uniform flow

This section is mainly performed to validate the IB-LBM FSI solver. The grid scale of the flow field is 600×300, a uniform flow is set to get through a channel with slip walls. The Reynolds number Re is 60 (the flexible filament can be activated to flap at such Re). The flexible filament is structured with the nodes-spring model, where the spacing of two adjacent nodes is 1.0 Δx. The stretching force is calculated with Eq. (3). The bending force is calculated by Eq. (4). The bending modulus K_b and the filament length L_p are set as variables. The boundary condition of the free end node is controlled by Eq. (5), and the simply supported end is controlled by [16,17]

$$\boldsymbol{X}=\ \boldsymbol{X}_0\ \text{and}\ \frac{\partial^2\boldsymbol{X}(s,t)}{\partial s^2}=0, \tag{21}$$

where $\boldsymbol{X}_0$ represents the fixed end. The penalty IB-LBM is adopted to calculate the inertial force of the filament [25], in which the filament itself is assumed to be massless, while a second ghost filament of a linear density m_s is attached through virtual springs. The spring force $\boldsymbol{F}_k$ is defined as

$$\boldsymbol{F}_k=K_v(\boldsymbol{Y}(s,t)-\boldsymbol{X}(s,t)), \tag{22}$$

where K_v is the stiffness of virtual springs (here set $K_v=0.3$), and $\boldsymbol{Y}(s,\ t)$ is the position of the ghost filament, it can be updated by

$$S\frac{\partial^2\boldsymbol{Y}(s,t)}{\partial t^2}=-\boldsymbol{F}_k. \tag{23}$$

We have conducted an experiment by using the similar method as [26,27], and captured three typical vibration patterns, as shown in Fig. 2(a2–c2). Numerical simulations with the parameters in Table 1 gave the consistent patterns, as shown in Fig. 2(a1–c1). In Table 1, the three dimensionless parameters are defined as below, the stretching coefficient $K_s=E_s/(\rho U^2\ L_p)$, the bending coefficient $K_b=E_b/(\rho U^2L_p^3)$ and the mass ratio $S=m_s/(\rho\ L_p)$, where E_s, E_b and m_s are respectively the corresponding parameters in LBM frame.

The results indicate that the mathematical model we have established is able to model the FSI of flexible filaments in a viscous flow.

Table 1
Parameters setting of the filament in simulation.

Case	Parameters		
	K_s	K_b	S
a1	0.25	1.56×10^{-4}	0.56
b1	0.25	2.22×10^{-4}	1.33
c1	0.25	5.56×10^{-5}	1.75

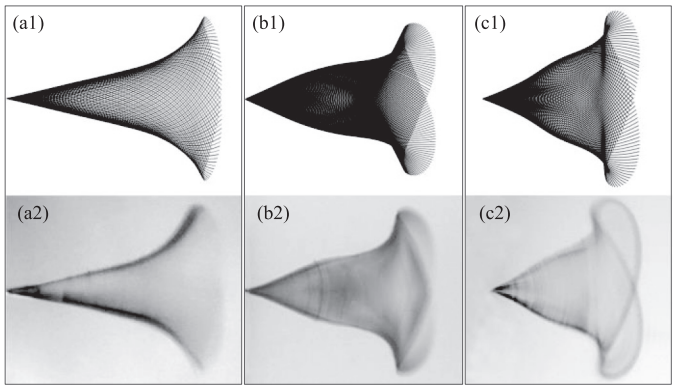

Fig. 2. Enveloping lines of a flapping flexible filament in a uniform flow.

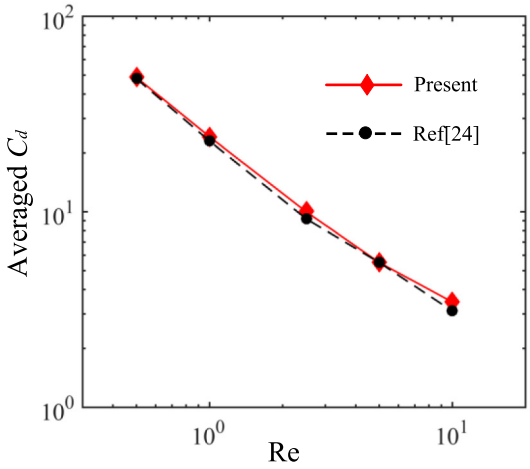

Fig. 3. Evolution of the averaged C_d with *Re*.

3.2. The flow past a compliant fiber tethered at the midpoint

In this section, the numerical example of flow past a compliant fiber tethered at the midpoint is introduced to verify the accuracy of our model [24,28], where the Reynolds number is set in the scope of 0.5 to 10, which has covered the problem we are going to discuss.

The fiber is structured with nodes-spring model, and the spacing of two adjacent nodes is $1.0\Delta x$. 51 nodes are set to construct the fiber; the length of the fiber is $L_p = 50$. The height $\times$ width of the channel is $8.4\,L_p \times 3.4\,L_p$, the initial position of the fiber is located at $6.4\,L_p$ away from the outlet (or $2\,L_p$ from the inlet). Set the dimensionless stretching coefficient $K_s = 20$, the dimensionless bending modulus $K_b = 0.013$, the additional dimensionless quantity $\eta = 6.2$. Other relevant parameters, definitions and boundary settings are set as the same to [24]. The logarithmic relationships between the averaged C_d of the fiber and *Re* are displayed in Fig. 3.

From Fig. 3, it is found that our results are in good accord with [24]. These results indicate that the model we have built is effective to deal with the FSI problem we are focusing on in this work.

4. Results and discussion

4.1. The focus pattern of the vibrating filament

According to the principle of momentum conservation, the filament will just vibrate steadily and symmetrically in an infinite area if setting $F_{dr,p} = -F_{dr,n}$ (in Fig. 1(a)). However, in our model, the filament is placed at a near-wall, our simulation results show that the filament vibrates asymmetrically and has a tendency to approach the wall gradually. In order to characterize the motion of the filament expediently, the movement path of the middle node $\boldsymbol{X}_m$ of the filament is recorded during its vibration and motion.

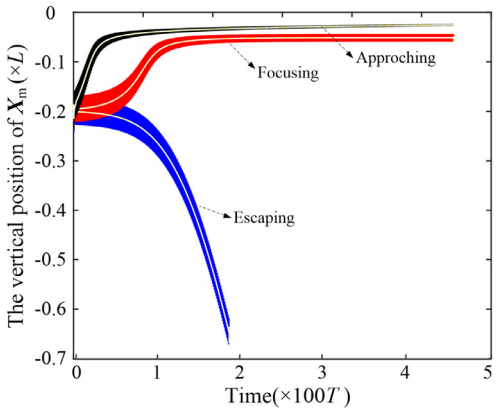

Fig. 4. The trajectories and A-A lines of $\boldsymbol{X}_{\mathrm{m}}$ for the focusing pattern and the escaping pattern. The white lines are the corresponding mean values.

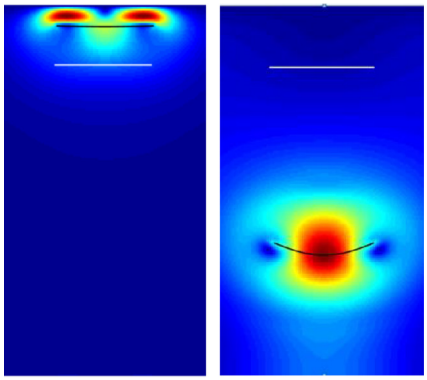

Fig. 5. Two snapshots of the migration patterns. (Left: focusing pattern; Right: escaping pattern). The white lines are the corresponding initial positions of the filament.

As shown in Fig. 4, three motion patterns are exhibited. The first is the black trajectory, in which the initial position of the filament is put $0.18\,L$ away from the upper wall, $F_{\mathrm{dr,p}}$ is set equal to $-F_{\mathrm{dr,n}}$, in this case, $\boldsymbol{X}_{\mathrm{m}}$ is found approaching the upper wall gradually, where the white line is the time-average value of the movement path of X_{m}, which is obtained by the smooth method of the adjacent-averaging with 20 points per window. For the convenience of description, we named the smoothed line as A-A line. The second is the red trajectory, where the initial position of the filament is also put $0.18\,L$ away from the upper wall. The difference is that the $F_{\mathrm{dr,p}}$ is regulated to be $-0.75 \times F_{\mathrm{dr,n}}$. Such set can produce an asymmetrical driving force on the two sides of the filament. The A-A line of the simulation result displays that the position of X_{m} experiences a slow rise at the beginning, then follows a fast growing, and finally reaches a stable state, we called this stable state as the focus pattern of the filament. Comparing with the second case, the third case just initializes the filament a little farther, that is $0.185\,L$ away from the wall. In this case, the filament is found departing from the wall rapidly, we called this process as the escaping pattern. In Fig. 5, the left frame is a snapshot from the focusing pattern and the right frame is from the escaping pattern, where the white lines represent the initial position of the filament, and the color map is the velocity field of flow.

To testify the stability of the focus pattern of the vibrating filament, by setting $F_{\mathrm{dr,p}} = -0.75 \times F_{\mathrm{dr,n}}$, three simulation cases by varying the initial positions are performed. According to the results, the A-A lines and vibrating amplitudes of $\boldsymbol{X}_{\mathrm{m}}$ are displayed in Fig. 6, where the three coarse line segments crossing the horizontal lines represent the respective scopes of the vibrating amplitude of $\boldsymbol{X}_{\mathrm{m}}$. The results show that three A-A lines come together with the time passing on, this indicates that there is only one focus position for all the three cases, and also reveals that the focus pattern of the vibrating filament is not sensitive to the initial position.

In addition, we also verify the grid independence. Here set $L_{\mathrm{p}} = 50$, 60 and 70 respectively, this will result in different grid scale because the grid of the flow filed is associated with the length of the filament L_{p}, as has been declared in Section 2.1, there is $L_{\mathrm{p}} = 0.25L$ and the grid scale of the flow field is $1.5\,L \times L$. The results in Fig. 7 show that the focusing processes of the filament are similar, and the focus positions are also close with each other. This demonstrates that $L_{\mathrm{p}} = 50$ and the corresponding grid scale are representative for the study of our FSI problem.

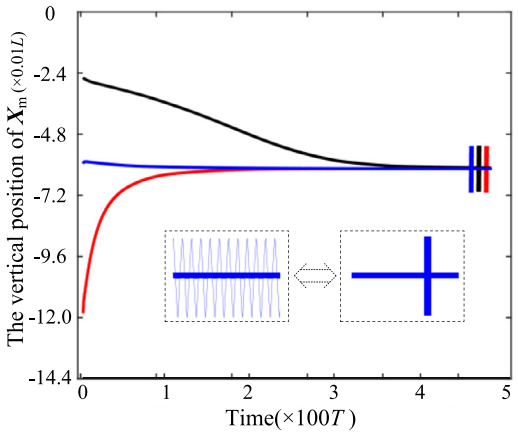

Fig. 6. The A-A lines and vibrating amplitudes of $\boldsymbol{X}_{\mathrm{m}}$ by varying the initial positions of the filaments.

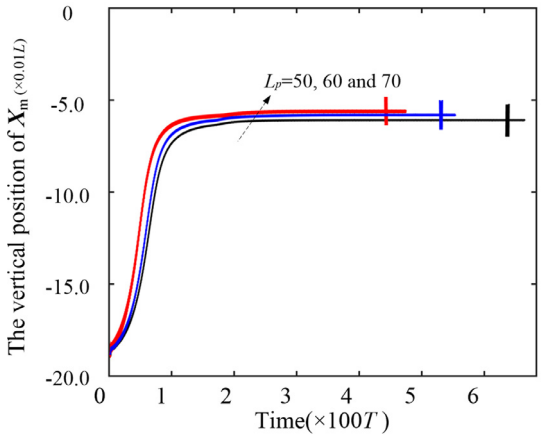

Fig. 7. The A-A lines and vibrating amplitudes of X_{m} by varying the grid scale.

4.2. The effect of boundary settings of the flow field on the focus

Here set $F_{\mathrm{dr,p}} = -0.75 \times F_{\mathrm{dr,n}}$, and three cases of boundary conditions are considered as the following. The first case (Case 1) is the acquiescent boundary setting. That is to set the upper boundary as wall, and the others are free flow boundaries. The second case (Case2) sets both the upper and the lower boundaries as walls, the left and right sides are free flow boundaries. The third case (Case 3) sets all boundaries as walls. The corresponding simulation results are shown in Fig. 8.

It is found that the three A-A lines of $\boldsymbol{X}_{\mathrm{m}}$ almost coincide with each other and the vibrating amplitudes are almost equivalent, this indicates that the upper wall is the critical boundary affecting the focus pattern of the vibrating filament.

4.3. Effect of the magnitude of $\mathrm{F}_{dr,p}$ *under an established* $\mathrm{F}_{dr,n}$

In order to explore the law between the focus pattern of filament and the driving force, we set $K = 0.90$, 0.85, 0.80, 0.75 and 0.70 in $F_{\mathrm{dr,p}} = -K \times F_{\mathrm{dr,n}}$ orderly, in which the magnitude of $F_{\mathrm{dr,n}}$ is fixed. By performing the simulations, the obtained A-A lines and vibrating amplitudes of $\boldsymbol{X}_{\mathrm{m}}$ are displayed in Fig. 9. There are two points that can be summarized from these results. First, the focus positions exhibit a regular tendency to depart from the upper wall by decreasing K, that is, a less $F_{\mathrm{dr,p}}$ will lead to a lower focus position. Second, the vibrating amplitude will experience a larger scope at a smaller K.

To exhibit the evolution law of the deformation of the filament, the enveloping lines of the vibration filament under $K = 0.85$, 0.80, 0.75 and 0.70 are displayed in Fig. 10, where the blue points are used to mark the middle node $\boldsymbol{X}_{\mathrm{m}}$.

In addition, the non-dimensional pressure evolution is also obtained through our model. As shown in Fig. 11, four snapshots at the moment t_1 to t_4 in one vibration period are picked up from the case of $K = 0.8$, where t_1 to t_4 are chosen around the four switching moments of the driving force. The non-dimensional pressure is computed by $P = (P^* - P_0^*)/(\rho U^2)$, where P^* is the pressure in LBM and P_0^* is the pressure in the quiescent flow field. From Fig. 11 we know that when activating $F_{\mathrm{dr,n}}$ (cases t_1 and t_2 in Fig. 11), the filament has a tendency to depart from the upper wall, a low pressure distribution between the wall and the filament comes into being. On the contrary, when activating $F_{\mathrm{dr,p}}$ (cases t_3 and t_4 in Fig. 11), the filament

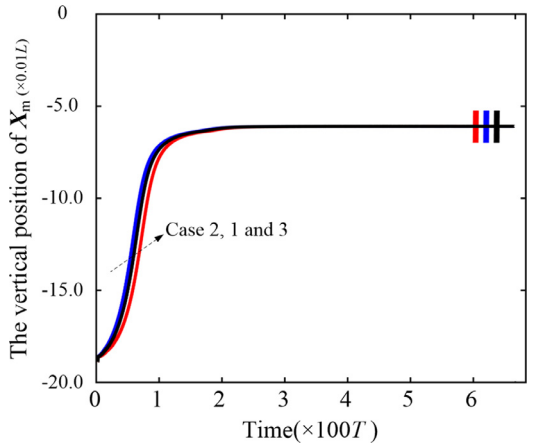

Fig. 8. The A-A lines and vibrating amplitudes of $\boldsymbol{X}_m$ under three cases of boundary condition settings.

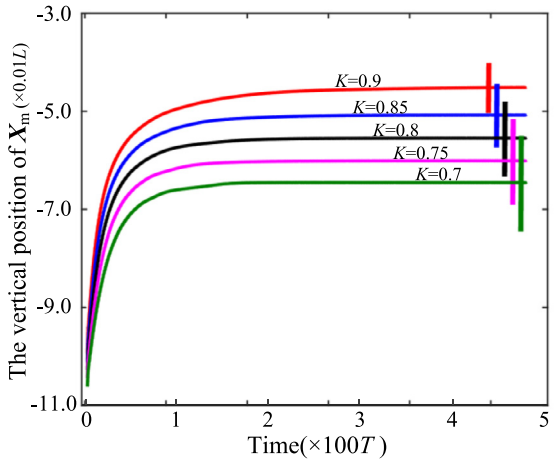

Fig. 9. The A-A lines and vibrating amplitudes of $\boldsymbol{X}_m$ by varying K. (The detail results are listed in Fig. 15(a)).

Table 2
Model settings and the effect of initialization of $\boldsymbol{F}_{dr}$.

Case	Grid scale	Boundary setting	Amplitude of F_{dr}	Initial filament position	Effects of the initialization of F_{dr}		
					$F_{dr,p}$-first	$F_{dr,n}$-first	Growing amplitude
A	$300 \times 200 (1.5L \times L)$	As in Section 2.3	$F_{dr,p} = -0.8 \times F_{dr,n}$	$0.1L$ to upper wall	No effect on final focus	No effect on final focus	No effect on final focus
B	300×600 $(1.5L \times 3L)$	All are periodic	$F_{dr,p} = -F_{dr,n}$	$0.1L$ to horizontal centerline	Migrate upward	Migrate downward	Get focused

is to move toward the upper wall, and a high pressure area arises. Therefore, the pressure of the fluid between the filament and the wall will experience a drastic change in a period of driving force, this implies that the pressure difference could be one important factor for the focus pattern of the filament, this will be discussed in the later part of force analysis.

4.4. Effect of the initialization of f_{dr}

In this section, we want to know if the initialization of the driving force $\boldsymbol{F}_{dr}$ has an effect on the migration of the vibrating filament. Two numerical cases marked as case A and case B are carried out to identify the effect. The grid scale, boundary setting, amplitude of $\boldsymbol{F}_{dr}$ and initial position for the two cases are listed in Table 2. Three settings of $\boldsymbol{F}_{dr}$, named as $F_{dr,p}$-first, $F_{dr,n}$-first and growing amplitude are applied to study the motion of the filament. In the setting of growing amplitude, the force magnitude increases linearly from 0 to the normal level during the first 10,000 time steps.

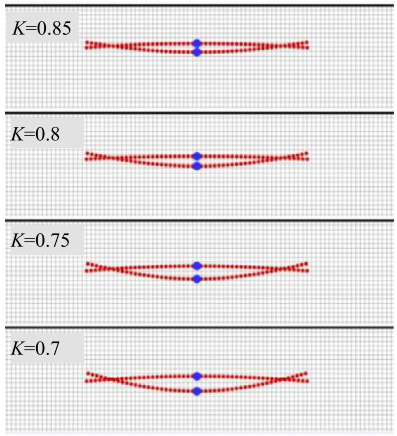

Fig. 10. The enveloping lines of the vibration filament.

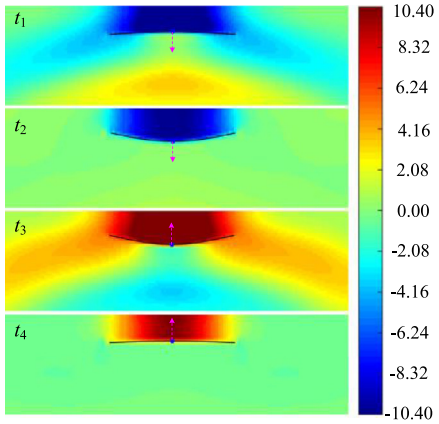

Fig. 11. The non-dimensional pressure at the moments from t_1 to t_4. The arrow denotes the moving direction of the filament at the present moment.

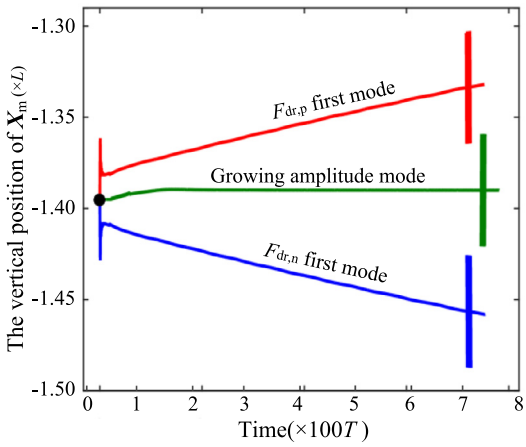

Fig. 12. The A-A lines and vibrating amplitudes of $\boldsymbol{X}_m$.

In case A, the A-A lines and vibrating amplitudes of X_m of the filament are found coming to the same level in the end. This makes it clear that there is little effect of the initialization of F_{dr} on the focus of the vibrating filament.

In case B, the grid scale in vertical direction is extended as 3 times as in model A, and all boundaries are set as periodic to simulate the flow field without a wall. The corresponding A-A lines and vibrating amplitudes of X_m are displayed in Fig. 12. In which the black point is the start point of $\boldsymbol{X}_m$. It is found that the three results are quite different. In $F_{dr,p}$-

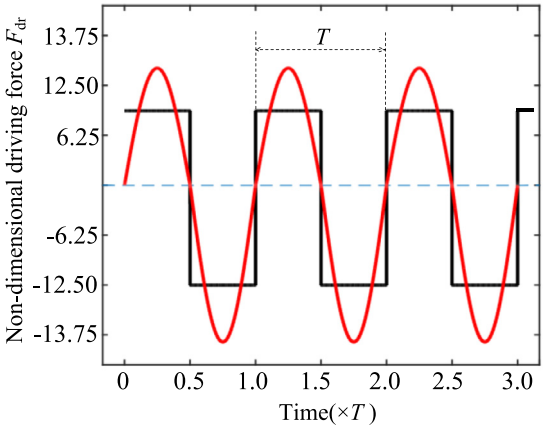

Fig. 13. The square and sine waveforms of the driving force.

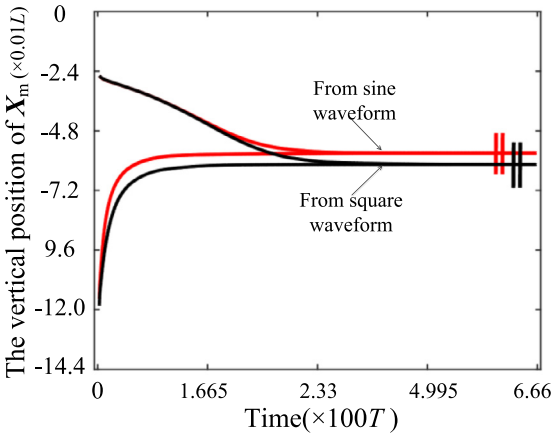

Fig. 14. The A-A lines and vibrating amplitudes of $\boldsymbol{X}_m$ of different waveforms of the driving force.

first mode, the driving force starts by $F_{dr,p}$, the vibrating filament is found migrating upward with a steady speed. On the contrary, in the $F_{dr,n}$-first mode, the driving force starts by $F_{dr,n}$, the vibrating filament migrates downward gradually. In the growing amplitude mode, the vibrating filament gets focused in the end. These results indicate the initialization of F_{dr} can influence the motion state of the filament in an infinite flow field.

4.5. Effect of the waveform and the period of f_{dr}

Two types of waveforms of $\boldsymbol{F}_{dr}$, the square wave and the sine wave are considered to study the motion of the filament, the settings of the waveform are displayed in Fig. 13. For each period of T, the previous half is the positive force component $F_{dr,p}$, and the latter half is the negative force component $F_{dr,n}$. As to the magnitudes of F_{dr}, set $F_{dr,p} = -0.75 \times F_{dr,n}$ for the square wave. In order to keep the statistic of F_{dr} to be a same level, the integration of $F_{dr,p}$ of the sine wave is set as the same to that of the square wave, as well as $F_{dr,n}$.

As a result, the A-A lines and vibrating amplitudes of $\boldsymbol{X}_m$ of the two types of driving force are shown in Fig. 14. The results reveal that although there is a bit of difference between the focus positions and amplitudes, the two types of waveforms of $\boldsymbol{F}_{dr}$ lead to the similar focus pattern.

In addition, the effect of the period of the square-wave driving force is also studied. Here set $F_{dr,p} = -0.8 \times F_{dr,n}$ and $T_0 = 6000\Delta t$, the period is set respectively as $0.6T_0$, $0.7T_0$, $0.8T_0$, $0.9T_0$ and $1.0T_0$. The simulation results are displayed in Fig. 15(b). It is found that with the extending of the period, the vibrating amplitude of the filament tends to increase, and the focus position of X_m has a tendency to approach the upper wall. The causations are analyzed as below. For the increase of the vibrating amplitude, it may be caused by the slower alternating of driving force, which means more accumulation of the filament migration in one vibrating period. For the change of the focus position of $\boldsymbol{X}_m$, we deduce that the growth of the driving force period and the vibrating amplitude may strengthen the attractive effect from the wall.

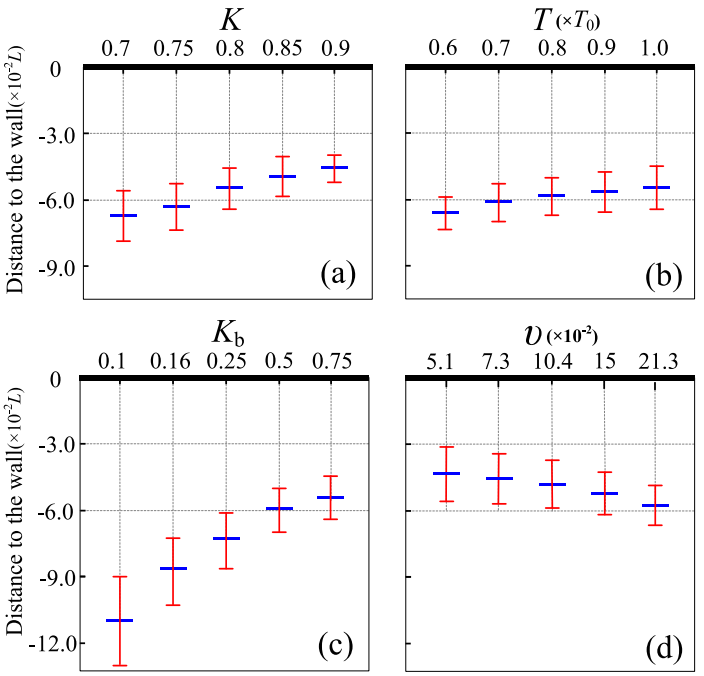

Fig. 15. The mean focus position (horizontal lines) and the vibrating amplitude (error bars) of $\boldsymbol{X}_{\mathrm{m}}$ under different variables.

4.6. Effect of the filament bending modulus

The bending modulus is a key factor for the deformation of the filament, it is significant to discuss the effect of the filament bending modulus on the motion of the vibrating filament. In this section, set $F_{\mathrm{dr,p}} = -0.8 \times F_{\mathrm{dr,n}}$ other parameter settings except the bending modulus K_{b} are set as declared in Section 2.1. The bending modulus K_{b} is set respectively as 0.1, 0.16, 0.25, 0.5 and 0.75 to study the motion of the filament.

The simulation results are displayed in Fig. 15(c), which indicate that under the same driving force, the focus position of the filament tends to approach the wall when increasing K_{b}. Moreover, larger vibrating amplitude is found at a lower K_{b}. By contrast, the evolution tendencies of the focus position and the vibrating amplitude are found analogical with the case just by decreasing the magnitude of $F_{\mathrm{dr,p}}$ as described in Section 4.3.

4.7. Effect of the fluid viscosity

Generally, the fluid viscosity is a critical property of an FSI model. In D2Q9 LBM model, the non-dimensional kinematic viscosity υ can be obtained by $\upsilon = c_s^2(\tau - 0.5)\triangle t$, in which the variation of the relaxation time τ should be limited in the scope of 0.5 to 3 to meet the usability of LBM. In the present study, set $F_{\mathrm{dr,p}} = -0.8 \times F_{\mathrm{dr,n}}$ and υ is set respectively as 0.051, 0.073, 0.104, 0.150 and 0.213. In order to ensure all cases to be full developed, the total time steps are extended to be 6×10^6. The simulation results are shown in Fig. 15(d), and two conclusions are drawn as below. First, the focus position tends to depart from the wall with the growth of υ, this means the attractive effect from wall becomes weaker as υ is enlarged. Second, the vibrating amplitude tends to decrease with the growth of υ, which indicates that higher viscosity can produce higher resistance against the motion of the filament.

4.8. Force analysis on the focus of the vibrating filament

The focus pattern of the vibrating filament is a typical dynamic equilibrium phenomenon, which implies a balance of joint force effect from filament mechanics and hydrodynamics. In this section, by employing the law of momentum conservation based on the Navier–Stokes equation, we analyze the comprehensive force effects acted on the filament, and attempt to explain the causation of the focus pattern.

As a typical FSI problem, the dynamic system we have built meets the law of momentum conservation, therefore it can be expressed by the Navier–Stokes equation as

$$\rho \frac{\partial \boldsymbol{u}}{\partial t} + \rho \boldsymbol{u} \cdot \nabla \boldsymbol{u} + \nabla P - \mu \nabla^2 \boldsymbol{u} = \boldsymbol{F}_{\mathrm{p}}^*, \tag{24}$$

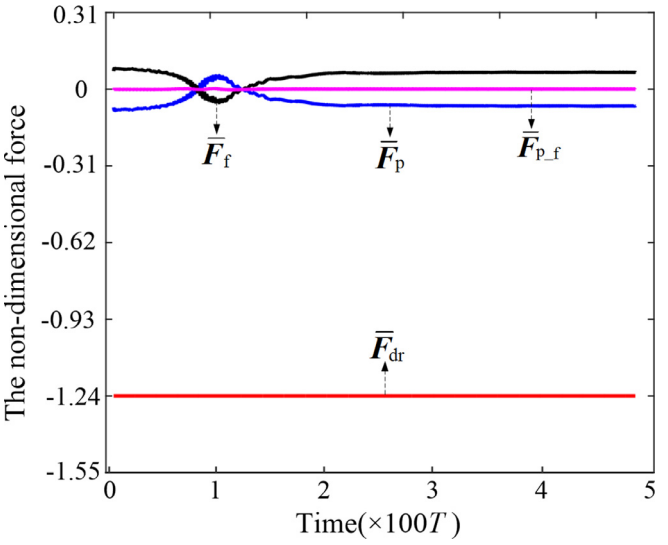

Fig. 16. The evolutions of the indices.

The left four items of Eq. (24) represent the kinetic effect of the flow, they are respectively the unsteady item, the convection item, the pressure item and the diffusion item. They are defined as four different indices as

$$\boldsymbol{F}_{f,1} = \int_{\Omega} \rho \frac{\partial \boldsymbol{u}(x,t)}{\partial t} \mathrm{d}x, \tag{25}$$

$$\boldsymbol{F}_{f,2} = \int_{\Omega} \rho \boldsymbol{u}(x,t) \cdot \nabla \boldsymbol{u}(x,t) \mathrm{d}x, \tag{26}$$

$$\boldsymbol{F}_{f,3} = \int_{\Omega} \nabla P(x,t) \mathrm{d}x, \tag{27}$$

$$\boldsymbol{F}_{f,4} = \int_{\Omega} -\mu \nabla^2 \boldsymbol{u}(x,t) \mathrm{d}x, \tag{28}$$

where Ω is the computational domain of the flow field. A negative combinational form of these four force items is defined as $\boldsymbol{F}_f$ by

$$\boldsymbol{F}_f = -\sum_{i=1}^{4} \boldsymbol{F}_{f,i}. \tag{29}$$

In Eq. (24), $\boldsymbol{F}_p^*$ is the resultant force on the filament nodes, the integration of the force on the filament is

$$\boldsymbol{F}_p = \int_0^{L_p} \boldsymbol{F}_p^*(s,t) \mathrm{d}s, \tag{30}$$

where L_p is the length of the filament.

To give an example to analyze the force effects of the filament focus, we pick up the case of $F_{dr,p} = -0.75 \times F_{dr,n}$ in Section 4.3, for which the A-A line of $\boldsymbol{X}_m$ is shown as the purple line (K=0.75) in Fig. 9. In order to make a convenient way to exhibit the effect of each index on the filament, an average non-dimensional form of a periodic force item is defined as

$$\bar{\boldsymbol{F}}_x(t) = \frac{1}{\rho U^2 L_p} \int_t^{t+0.5T} \frac{\boldsymbol{F}_x(\xi)}{0.5T} d\xi, \tag{31}$$

where T is the period of the driving force $\boldsymbol{F}_{dr}$.

By using Eq. (31), the periodic driving force $\boldsymbol{F}_{dr}$ is transformed into a constant $\bar{\boldsymbol{F}}_{dr}$. $\bar{\boldsymbol{F}}_{dr}$ can be viewed as a statistical index of $\boldsymbol{F}_{dr}$ on time axis. Correspondingly, $\bar{\boldsymbol{F}}_p$ is the transform of $\boldsymbol{F}_p$ and $\bar{\boldsymbol{F}}_f$ is the transform of $\boldsymbol{F}_f$. In addition, define $\bar{\boldsymbol{F}}_{p\_f} = \bar{\boldsymbol{F}}_p + \bar{\boldsymbol{F}}_f$. Then the corresponding evolution lines of $\bar{\boldsymbol{F}}_{dr}$, $\bar{\boldsymbol{F}}_p$, $\bar{\boldsymbol{F}}_f$ and $\bar{\boldsymbol{F}}_{p\_f}$ are displayed in Fig. 16.

In Fig. 16, $\bar{\boldsymbol{F}}_{dr}$ is fixed at -1.24, it represents the statistical driving force tends to migrate the filament away the wall. However, $\bar{\boldsymbol{F}}_p$, the average joint force of the filament, which is composed of $\bar{\boldsymbol{F}}_{dr}$, $\bar{\boldsymbol{F}}_s$ ($\boldsymbol{F}_s$ is the stretching force on filament nodes) and $\bar{\boldsymbol{F}}_b$ ($\boldsymbol{F}_b$ is the bending force on the filament modes), is found much closer to zero level compared to $\bar{\boldsymbol{F}}_{dr}$. This indicates that the stretching force and the bending force of the filament eliminate the vast majority of the effect of $\bar{\boldsymbol{F}}_{dr}$.

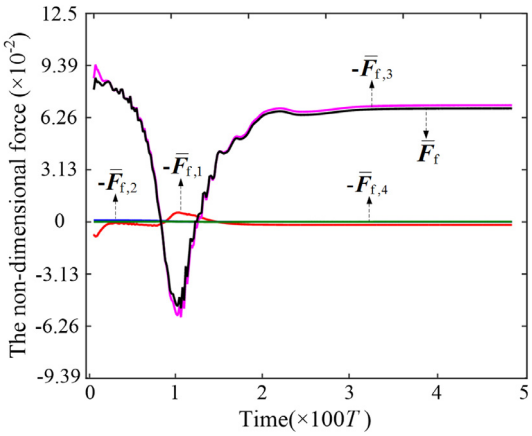

Fig. 17. The contributions of each item of $-\bar{\boldsymbol{F}}_{\mathrm{f},1}$ to $-\bar{\boldsymbol{F}}_{\mathrm{f},4}$ to the comprehensive kinetics effect of the flow.

Moreover, different from obtaining $\bar{\boldsymbol{F}}_{\mathrm{p}}$, $\bar{\boldsymbol{F}}_{\mathrm{f}}$ is extracted from the overall flow filed (its curve color is black in Fig. 16). By comparing $\bar{\boldsymbol{F}}_{\mathrm{p}}$ with $\bar{\boldsymbol{F}}_{\mathrm{f}}$, there is $\bar{\boldsymbol{F}}_{\mathrm{p}} \approx -\bar{\boldsymbol{F}}_{\mathrm{f}}$. Therefore we know $\bar{\boldsymbol{F}}_{\mathrm{p\_f}} \approx 0$ ($\bar{\boldsymbol{F}}_{\mathrm{p\_f}} = \bar{\boldsymbol{F}}_{\mathrm{p}} + \bar{\boldsymbol{F}}_{\mathrm{f}}$), as displayed by the purple line in Fig. 16. This demonstrates that Eq. (24) is well satisfied.

According to the variation tendencies of $\bar{\boldsymbol{F}}_{\mathrm{p}}$ and $\bar{\boldsymbol{F}}_{\mathrm{f}}$, it is found that the steady $\bar{\boldsymbol{F}}_{\mathrm{p}}$ or $\bar{\boldsymbol{F}}_{\mathrm{f}}$ corresponds to the stable focus state of the filament. Therefore, we infer that the focus pattern of the vibrating filament may be caused by such condition that $\bar{\boldsymbol{F}}_{\mathrm{p}}$ and $\bar{\boldsymbol{F}}_{\mathrm{f}}$ do not vary any more with the time passing on. Moreover, it is also found that the focus pattern is accompanied by stable nonzero values of $\bar{\boldsymbol{F}}_{\mathrm{p}}$ and $\bar{\boldsymbol{F}}_{\mathrm{f}}$, this imply that there is a balance between the two indices, just such balance determine the focus pattern of the vibrating filament.

Besides, in order to discover the detail of the mechanism of the vibrating filament, it is necessary to know what the actual effects are for each component of $\bar{\boldsymbol{F}}_{\mathrm{f}}$. According to the simulation results, the evolution lines of $-\bar{\boldsymbol{F}}_{\mathrm{f},1}$ to $-\bar{\boldsymbol{F}}_{\mathrm{f},4}$ and $\bar{\boldsymbol{F}}_{\mathrm{f}}$ are displayed in Fig. 17. It is found that $-\bar{\boldsymbol{F}}_{\mathrm{f},2}$ and $-\bar{\boldsymbol{F}}_{\mathrm{f},4}$ almost keep at zero level in the whole process, and $-\bar{\boldsymbol{F}}_{\mathrm{f},1}$ varies in a small range at the beginning, then gets steady on a level near to zero. By contrast, $-\bar{\boldsymbol{F}}_{\mathrm{f},3}$ experiences a large variation and $\bar{\boldsymbol{F}}_{\mathrm{f}}$ is found quite close to $-\bar{\boldsymbol{F}}_{\mathrm{f},3}$, this indicates that the pressure is the leading component of $\bar{\boldsymbol{F}}_{\mathrm{f}}$; this conclusion also provides an apt verification for the deduction made for Fig. 11 in Section 4.3.

According to the above analysis, we conclude that the focus pattern of the vibrating filament is mainly caused by the balance between the joint force on the filament and the pressure from the flow filed. We think this is compatible to explain the causation of wall attraction.

5. Conclusion

In this paper, to explore the mechanism of wall attraction of micro-swimmers, we performed a numerical study on an external-force induced focus pattern of a vibrating flexible filament in a viscous fluid. The laws of the focus pattern we have found are listed as below. First, the crucial boundary is the near-wall, the effect from other boundaries of the flow field is very small. Second, the square and the sine waveforms of the driving force can produce the similar focus pattern. Third, decrease the driving force magnitude of the wall side or the bending modulus of the filament will enlarge the vibrating amplitude and result in a tendency to depart from the wall. Fourth, decrease in the period of the driving force will lead to smaller vibrating amplitude, while the focused filament will keep a larger distance from the wall. Finally, a decrease in the fluid viscosity can obtain the whole reverse tendencies of decreasing the force period. By conducting the hydrodynamic analysis, we show that the focus pattern of the vibrating filament and the corresponding wall attraction phenomenon are mainly caused by the balance between the joint force on the filament and the pressure from the flow field. Therefore, our study may give an essential explanation on the hydrodynamic mechanism of sperm accumulation.

Acknowledgment

This work is supported by the National Natural Science Foundation of China (No. 81771935 and No. 81471743). Dr. F.-B. Tian is the recipient of an Australian Research Council Discovery Early Career Researcher Award (project number DE160101098).

References

[1] E. Lauga, T.R. Powers, The hydrodynamics of swimming microorganisms, Rev. Prog. Phys 72 (2009) 096601.
[2] X.N. Shen, P.E. Arratia, Undulatory swimming in viscoelastic fluids, Phys. Rev. Lett. 106 (2011) 208101.

[3] F. Alouges, A. DeSimone, L. Giraldi, M. Zoppello, Can magnetic multilayers propel artificial microswimmers mimicking sperm cell, Soft Robot 2 (2013) 117–129.
[4] L. Rothschild, Non-random distribution of bull spermatazoa in a drop of sperm suspension, Nature 198 (1963) 1221–1222.
[5] D.J. Smith, E.A. Gaffney, J.R. Blake, et al., Human sperm accumulation near surfaces: a simulation study, J. Fluid Mech. 621 (2009) 289–320.
[6] L.J. Fauci, R. Dillon, Biofluid mechanics of reproduction, Annu. Rev. Fluid Mech. 38 (2006) 371–394.
[7] F.H. Qin, W.X. Huang, H.J. Sung, Simulation of small swimmer motions driven by tail/flagellum beating, Comput. Fluids 55 (2012) 109–117.
[8] P. Denissenko, V. Kantsler, D.J. Smith, et al., Human spermatozoa migration in microchannels reveals boundary-following navigation, PNAS 109 (21) (2012) 8007–8010.
[9] H. Winet, G.S. Bernstein, J. Head, Observations on the response of human spermatazoa to gravity, boundaries and fluid shear, J. Reprod. Fertil. 70 (1984) 511–523.
[10] L.J. Fauci, A. McDonald, Sperm motility in the presence of boundaries, Bull. Math. Biol. 57 (5) (1995) 679–699.
[11] J. Elgeti, U. Kaupp, G. Gompper, Hydrodynamics of sperm cells near surfaces, Biophys. J. 99 (2010) 1018–1026.
[12] Y.Q. Xu, X.Y. Tang, F.B. Tian, et al., IB-LBM simulation of the haemocyte dynamics in a stenotic capillary, Comput. Methods Biomech. Biomed. Eng. 17 (9) (2014) 978–985.
[13] Q. Wei, Y.Q. Xu, F.B Tian, et al., IB-LBM simulation on blood cell sorting with a micro-fence structure, Bio-Med. Mater. Eng. 24 (1) (2014) 475–481.
[14] F.B. Tian, FSI modeling with the DSD/SST method for the fluid and finite difference method for the structure, Comput. Mech. 54 (2) (2014) 581–589.
[15] L.D. Zhu, C.S. Peskin, Simulation of a flapping flexible filament in a flowing soap film by the immersed boundary method, J. Comput. Phys. 179 (2) (2002) 452–468.
[16] F.B. Tian, Y. Wang, J. Young, J.C.S. Lai, An FSI solution technique based on the DSD/SST method and its applications, Math. Models Methods Appl. Sci. 25 (12) (2015) 2257–2285.
[17] F.B. Tian, H.X. Luo, J.L Song, et al., Force production and asymmetric deformation of a flexible flapping wing in forward flight, J. Fluids Struct. 36 (2013) 149–161.
[18] Y.Q. Xu, F.B. Tian, Y.L. Deng, An efficient red blood cell model in the frame of IB-LBM and its application, Int. J. Biomath. 06 (01) (2013) 1250061.
[19] C.L. Chen, S.C. Chang, C.K. Chen, et al., Lattice Boltzmann simulation for mixed convection of nanofluids in a square enclosure, Appl. Math. Model. 39 (8) (2015) 2436–2451.
[20] C.K. Aidun, J.R. Clausen, Lattice-Boltzmann method for complex flows, Annu. Rev. Fluid Mech. 42 (2010) 439–472.
[21] Z.L. Guo, C.G. Zheng, B.C. Shi, Discrete lattice effects on the forcing term in the lattice Boltzmann method, Phys. Rev. E 65 (4) (2002) 046308.
[22] Y.B. Gan, A.G. Xu, S. Zhang, Succi discrete Boltzmann modeling of multiphase flows: hydrodynamic and thermodynamic non-equilibrium effects, Soft Matter 11 (2015) 5336–5345.
[23] C.S. Peskin, The immersed boundary method, Acta Numer. 11 (2002) 479–517.
[24] L.D. Zhu, Scaling laws for drag of a compliant body moving in an incompressible viscous fluid, J. Fluid Mech. 607 (2008) 387–400.
[25] F.B. Tian, H.X. Luo, L.D Zhu, et al., An efficient immersed boundary-lattice Boltzmann method for the hydrodynamic interaction of elastic filaments, J. Comput. Phys. 230 (19) (2011) 7266–7283.
[26] J. Zhang, S. Childress, A. Libchaber, et al., Flexible filaments in a flowing soap film as a model for one-dimensional flags in a two-dimensional wind, Nature 408 (2000) 835–839.
[27] C.-Y. Bao, C. Tang, X.-Z. Yin, et al., Flutter of finite-span flexible plates in uniform flow, Chin. Phys. Lett. 27 (2010) 064601.
[28] S. Alben, M. Shelley, J Zhang, Drag reduction through shelf-similar bending of a flexible body, Nature 420 (6915) (2002) 479–481.